Received: 5 June 2016 | Revised: 30 July 2016 | Accepted: 4 August 2016

DOI: 10.1002/cmr.b.21326

RESEARCH ARTICLE

WILEY

Subject-loaded quadrifilar helical-antenna RF coil with high B_1^+ field uniformity and large FOV for 3-T MRI

Pranav S. Athalye[1] | Nada J. Šekeljić[1,2] | Milan M. Ilić[1,3] | Alexey A. Tonyushkin[4,5] | Branislav M. Notaroš[1]

[1]Department of Electrical and Computer Engineering, Colorado State University, Fort Collins, CO, USA

[2]Intel Corporation, Hillsboro, OR, USA

[3]School of Electrical Engineering, University of Belgrade, Belgrade, Serbia

[4]Physics Department, University of Massachusetts Boston, Boston, MA, USA

[5]Radiology Department, Massachusetts General Hospital, Boston, MA, USA

Correspondence
B. M. Notaroš, Department of Electrical and Computer Engineering, Colorado State University, Fort Collins, CO, USA.
Email: notaros@colostate.edu

Abstract

A novel method for excitation of RF B_1 field in high-field (3-T) magnetic resonance imaging (MRI) systems using a subject-loaded quadrifilar helical antenna as an RF coil is proposed, evaluated, and demonstrated. Design, analysis, characterization, and evaluation of the novel coil when situated in a 3-T MRI bore and loaded with different phantoms are performed and cross-validated by extensive numerical simulations using multiple computational electromagnetics techniques. The results for the quadrifilar helical-antenna RF body coil show (a) strong field penetration in the entire phantoms; (b) excellent right-hand circular polarization (RCP); (c) high spatial uniformity of RCP RF magnetic field, B_1^+, throughout the phantoms; (d) large field of view (FOV); (e) good transmit efficiency; and (f) low local specific absorption rate (SAR). The examples show that the new RF coil provides substantially better B_1^+-field uniformity and much larger FOV than any of the previously reported numerical and experimental results for the existing RF coil designs at 3 T in literature that enable comparison. In addition, helical RF body coils of different lengths can, for instance, easily provide an excellent RCP and highly uniform B_1^+-field within the MRI maximum FOV length of 50 cm, and even 100 cm. The proposed MRI RF coil yields a remarkable improvement in the field uniformity in the longitudinal direction, for various phantoms, with comparable efficiency and SAR levels.

KEYWORDS

B_1^+ field uniformity, high-field 3-T MRI systems, magnetic resonance imaging (MRI), quadrifilar helical-antenna coil, RF body coils

1 | INTRODUCTION

Magnetic resonance imaging (MRI) is an established medical diagnostic method and tool widely utilized to obtain high-resolution images of the internal structure of the body or its parts and organs. The physical foundation of MRI is the principle of nuclear magnetic resonance (NMR), whereby atom nuclei of the tissue that is imaged absorb and reemit applied radio frequency (RF) radiation based on the resonant frequency with which the spin precesses in an external polarizing static (dc) magnetic field (magnetic flux density), B_0, the so-called Larmor frequency, f_0, that is proportional to B_0.[1–3] In an MRI scanner, the main polarizing static field $\mathbf{B}_0$ is generated by the main coil known as magnet, and its direction is longitudinal, along the MRI bore, i.e., along the z-axis. Note that in this work, vectors (real or complex) are represented by boldface, regular (non-italic) symbols, e.g., $\mathbf{B}$, whereas the magnitudes of vectors are denoted by italic, nonbold symbols, e.g., B. While the terminology largely varies, the 3-T scanners ($B_0 = 3$ T) are usually referred to as the high-field or very high-field magnets, with the low-field systems and mid-field systems being those with $B_0 < 3$ T. The MRI machines

with $B_0 > 3$ T are considered the ultrahigh-field systems.[4] In addition to the static field, gradient coils create magnetic field gradients that vary the resonant frequency in space and time, which facilitates MRI.

An RF excitation magnetic field, $\mathbf{B}_1$, is applied in orthogonal direction to the main polarizing field, and it creates a transverse magnetization that induces a time-dependent signal in the receive coil. For maximum coupling between the RF field and the spins in the tissue, a rotating magnetic field with constant magnitude during rotation is desired, i.e., the RF exciter needs to generate a circularly polarized (CP), and more precisely, right-hand CP (RCP) RF magnetic field, usually denoted as $\mathbf{B}_1^+$.

Despite the fact that the MRI scanner at clinical field strengths, $B_0 = 1.5$ T, and even $B_0 = 3$ T, is considered to be a developed technology, there still are a number of engineering challenges associated with the design of an optimal RF coil. The principal desired objectives for the development and design of RF coils and $\mathbf{B}_1$ fields inside an MRI bore loaded with a human or phantom can be summarized as follows. First, there should be a strong coupling of the field with a subject and deep field penetration into the tissues. Second, a good circular polarization, and more precisely, RCP, of the $\mathbf{B}_1$ field for the transverse components (normal to the axis of the bore and to field $\mathbf{B}_0$) of $\mathbf{B}_1$ in the subject should be achieved. This means a very predominant RCP component of the transverse $\mathbf{B}_1$, B_1^+, over the left-hand CP (LCP) component, B_1^-, and hence a high ratio B_1^+/B_1^-. Purely CP $\mathbf{B}_1$ field, with $B_1^- = 0$ and equal powers in the two transverse components (x and y components), is desirable. The more circularly polarized $\mathbf{B}_1$ field, the higher the transmit efficiency that results into higher signal-to-noise ratio (SNR). A linearly polarized (LP) field would require too much RF deposition into the subject to get the same SNR as compared to a modest power with a CP $\mathbf{B}_1$ field. Hence, LP $\mathbf{B}_1$ fields are undesirable. Third, a high spatial uniformity of the transverse $\mathbf{B}_1^+$ field along the z-axis, large field of view (FOV), and as uniform as possible RCP transverse field, $\mathbf{B}_1^+$, elsewhere in the subject are desired. Transverse $\mathbf{B}_1^+$ field uniformity is directly related to the resulting MRI image quality. It is relatively easy for the polarizing static field $\mathbf{B}_0$ to be shimmed to very high uniformity using shim coils ($\mathbf{B}_0$ shimming is done automatically during system initialization prior to imaging), so that any image nonuniformity is due to the transverse $\mathbf{B}_1^+$ field nonuniformity. The last requirement is that the local specific absorption rate (SAR) at every point in the body, found as $\sigma(\mathbf{r})|\mathbf{E}(\mathbf{r})|^2/\rho(\mathbf{r})$, in units of W/kg = mW/g, with σ standing for the conductivity (the unit is S/m) and ρ for the mass density (kg/m^3) of the material (tissue), $\mathbf{E}$ for the electric field intensity vector (V/m), and $\mathbf{r}$ for the position vector of the point inside the body, as well as averaged total SAR values for individual organs and body areas, must be, for the given total input RF power of the system, well below the acceptable and allowable prescribed SAR levels, to prevent any potential health hazards.

State-of-the-art clinical MRI scanners are 3-T systems ($B_0 = 3$ T), i.e., high-field magnets, with MRI bores measuring typically 60 cm in diameter, which allows full-body human subjects. However, 3-T scanners are yet far from constituting a majority of MRI machines in hospitals, where 1.5-T scanners still prevail by a very large margin in part due to higher costs but also due to field inhomogeneity issues, SAR constraints, etc. In 3-T clinical, preclinical, and research MRI scanners, the RF exciter is almost exclusively in the form of a birdcage coil.[5] While birdcage body coils are mostly used only as RF transmitters with local surface coils as receivers, smaller birdcage coils[6] (e.g., head and extremity coils), which are closer to the imaged objects/tissues, are often used as both RF transmitters and receivers.

Several recent attempts to improving $\mathbf{B}_1^+$ field uniformity of body coils in preclinical scanners at high and ultrahigh fields ($B_0 \geq 3$ T) include various modifications of the birdcage coil, such as a birdcage coil with detached endcaps,[7] TEM coils,[8–10] and spiral coils.[11] The system proposed in Ref. 7 significantly improves the field uniformity in longitudinal direction [note that the FOV is within approximately 20 cm (in the head region)]. The phased array TEM coil for whole-body imaging[9] reduces B_1^+ nonuniformity and suppresses the SAR level. In, Ref. 11 twisting a birdcage coil structure toward a spiral shape is used to distribute the RF phase through space and improve the field uniformity, for head RF excitation at 4 T. Solutions that exploit possible traveling waves in MRI systems at $B_0 \geq 7$ T include patch antennas that excite LP or CP traveling-wave fields inside a scanner's bore.[12] This excitation, however, if not aided by additional electrodynamic elements (dielectrics or metamaterials), is highly localized, which results in rapid power dissipation in the body and quick attenuation with distance away from the antenna. In addition, the traveling-wave concept has been mostly invoked and tested in 60-cm MRI bores at 7 T.[13–15] On the other hand, there exist several traveling-wave-inspired designs at 3 T employing a parallel-plate waveguide,[16] dielectric inserts,[17] and a cylindrical metallic waveguide as an RF shield,[18] respectively, to facilitate RF field coupling to the subject.

In fact, the main area of engineering research in advancing next-generation MRI scanners at high ($B_0 = 3$ T) and ultrahigh ($B_0 > 3$ T) polarizing fields is in improving RF coils and $\mathbf{B}_1$ fields in a MRI bore loaded with a human body or a phantom.

Here, we propose and numerically validate, evaluate, and demonstrate a novel method for excitation of RF B_1 field in high-field MRI systems, with $B_0 = 3$ T and Larmor frequency of $f_0 = 127.8$ MHz, so for state-of-the-art clinical scanners, using a subject-loaded quadrifilar helical antenna as an RF coil. Our full-wave electromagnetic simulations of 3-T MRI systems with phantom-loaded helical antennas

show efficient coupling and deep field penetration into the phantoms, high B_1^+/B_1^- ratio and spatial uniformity throughout the phantoms, large FOV, good transmit efficiency, and low SAR levels at every point in the phantom. Overall, the novel RF coil provides substantially better B_1^+ field uniformity and much larger FOV than any of the previously reported results in literature that enable comparison. Moreover, it shows great potential for whole-body imaging[19] at 3 T, i.e., for MRI of the whole human body in a 3-T clinical system.

In principle, the novel method for RF excitation in MRI systems using a quadrifilar helical RF coil with high B_1^+ field uniformity and large FOV is universal and not limited to any particular field strength (B_0) and any particular frequency (f_0). However, comprehensive designs and full demonstrations of quadrifilar helical RF coils at fields other than 3 T are yet to be done as part of our future work. Furthermore, although the emphasis in this study is on examples proposing and demonstrating the quadrifilar helical antenna as an RF body coil, it can readily and favorably be used as a head coil or an extremity coil or a coil for abdominal scan, as well as for animal scanners.

The basic idea of the novel method for RF excitation at high and ultrahigh fields by means of quadrifilar helical antennas as RF body coils and initial results at both 3 T and 7 T are preliminary presented in a summary form in Refs 20–23. A subject-loaded monofilar axial-mode helical antenna as an RF exciter for 7-T MRI systems is preliminary presented in a summary form in Ref. 24.

Design, analysis, characterization, and evaluation of the proposed quadrifilar helical exciter when situated in a 3-T MRI bore and loaded with different phantoms is performed by extensive numerical simulations using a higher-order full-wave computational electromagnetics (CEM)[25] technique based on the method of moments in the surface integral equation formulation.[26] Whereas only MRI experiments will ultimately validate the properties and confirm the practical relevance of the new coil, we have made sure that all the simulation results presented in this study are rigorously checked and evaluated from all relevant numerical and modeling aspects, as well as thoroughly verified and validated by comparison with results using two well-established commercial full-wave CEM codes. The presented simulation results are very accurate and fully representative and predictive of the performance of the proposed RF coil in the actual MRI bore.

The here reported work proposes a novel idea of a subject-loaded quadrifilar helical-antenna RF coil for 3-T MRI. This study presents its design, characterization, and performance using CEM simulations. It demonstrates the proof of concept and introduces the intriguing approach of a four-channel helical RF body coil, with high B_1^+ field uniformity and large FOV, at 3 T. In the presented examples, the proposed coil is compared with the 3-T MRI scanners with the existing RF coil designs, in the cases where the reported results for these designs provide sufficient information for a meaningful comparison. The proposed system differs in concept to the existing ones; hence, our results indicate that it promises to complement the currently used solutions for 3-T MRI scanners and that it, therefore, provides an avenue well worth further exploration.

2 | METHODS

A helical antenna represents a metallic wire antenna wound uniformly and periodically with N wire turns and a pitch P about an imaginary (or dielectric) cylinder of diameter D_{helix} and length $L_{\text{helix}} = NP$,[27] and it is shown as Helix 1 (a single filament) in Fig. 1. The pitch P relates to the pitch angle, α, as $P = C_{\text{helix}} \tan \alpha$, where $C_{\text{helix}} = \pi D_{\text{helix}}$ is the helix circumference. The antenna is fed at one wire end against a circular back-plate, acting as a ground plane, i.e., the input power is supplied at a lumped excitation port [a delta-function generator][26] between the wire end and the plate. For the practical MRI RF excitation at 3 T, we specifically propose a four-channel helical RF coil—with high B_1^+ field uniformity and large FOV. The proposed coil is a quadrifilar helical antenna, where four helices (Helices 1–4 in Fig. 1) are wound

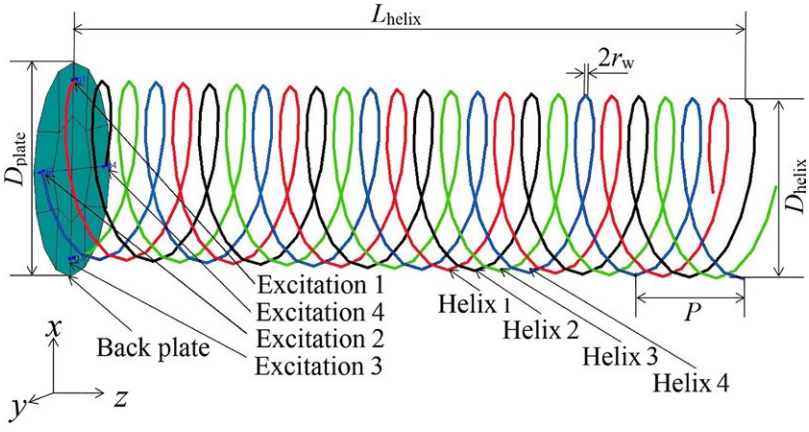

FIGURE 1 Quadrifilar helical antenna in free space. The antenna consists of four helices (Helices 1–4) fed by four delta-function generators (Excitations 1–4) with complex RMS voltages $V + j0$, $0 - jV$, $-V + j0$, and $0 + jV$, respectively

coaxially and fed in time-phase quadrature, i.e., by 90° out of phase with respect to each other (with complex voltages of delta-function generators equaling $V + \mathrm{j}0$, $0 - \mathrm{j}V$, $-V + \mathrm{j}0$, and $0 + \mathrm{j}V$, respectively, where $\mathrm{j} = \sqrt{-1}$ is the imaginary unit), against the common back-plate, so their currents flow along the wires in time-phase quadrature.

Design of the proposed quadrifilar helical exciters, as well as analysis of the RF electromagnetic field in 3-T MRI bores generated by the exciters, are performed using a full-wave numerically rigorous CEM technique based on the method of moments (MoM) in conjunction with the surface integral equation (SIE) approach,[26] implemented in a numerically higher-order fashion.[25] In this technique, all material (metallic and dielectric) surfaces in the structure are modeled using generalized parametric quadrilateral patches and all metallic wires are modeled by means of straight wire segments, electric and magnetic equivalent surface currents over elements (quadrilateral patches and wire segments) are modeled by polynomial vector basis functions, and SIEs based on boundary conditions for electric and magnetic field vectors are solved employing Galerkin method.[26] In addition, the results obtained by the higher-order MoM-SIE technique are thoroughly verified and validated by comparison with results using two well-established commercial full-wave CEM codes, a MoM code WIPL-D,[28] and a finite element method (FEM) code ANSYS HFSS.[29]

To demonstrate the novel method for RF excitation using a subject-loaded helical antenna as an RF exciter at 3 T, Fig. 2 shows a 3-T system with a bore in the form of a metallic cylinder of diameter $D_{\mathrm{bore}} = 60$ cm and length $L_{\mathrm{bore}} = 200$ cm (simplified model of a clinical scanner). The bore is coaxially and centrally loaded with a phantom in the form of a cylinder of diameter D_{P} and length L_{P} filled with a homogeneous lossy dielectric of relative permittivity ε_{r}, conductivity σ, and relative permeability μ_{r}=1. Note that in MRI-related experiments and simulations, a phantom is a container of an arbitrary (but usually simple) shape, most commonly a cylindrical bottle, that is filled with a fluid resembling relative permittivity (dielectric constant) and conductivity parameters of human tissues and has NMR active species such as hydrogen molecules, e.g., saline water or deionized (DI) water. To prevent abrupt field changes and wave reflections at the ends of the phantom due to abrupt material discontinuities between the phantom medium and surrounding air, the phantom is terminated at each end with a cylindrical buffer of length L_{B} and the same diameter, $D_{\mathrm{B}} = D_{\mathrm{P}}$, made of the same material as the phantom (Fig. 2).

The RF magnetic field $\mathbf{B}_1$ in the bore and in the phantom is excited by a phantom-loaded quadrifilar helical antenna, of diameter D_{helix} and length L_{helix}, with the pitch and wire radius of each of the four helices being P and r_{w}, respectively, placed coaxially with respect to the bore and the phantom and fed as in Fig. 1, against the back-plate of diameter D_{plate}, at an operating frequency of $f_0 = 127.8$ MHz. In addition to a solid back-plate, we also implement designs with a hollow back-plate (metallic ring) of outer and inner diameters D_{plate1} and D_{plate2}, respectively. Namely, in clinical applications, a solid back-plate closing off one end of the MRI bore may be impractical, and the hollow one may be preferred to provide more comfort to the patient and better access to the bore. In addition, strong surface eddy currents induced on a continuous plate may generate RF noise, which, if the plate is close to the subject, may adversely affect the SNR of the image; these currents may even cause strong mechanical vibration of the plate and loud acoustic noise during the scan, due to the changing magnetic gradient.

In terms of further improvements of the designs, parameters of the helical antenna, e.g., the helix pitch, diameter, and length, can be varied and optimized for even better performance of the 3-T MRI system. Different feeding patterns and terminations of helices are also possible, as well as tapering of the windings. Multifilar antennas can also be designed and implemented to utilize parallel imaging.[30]

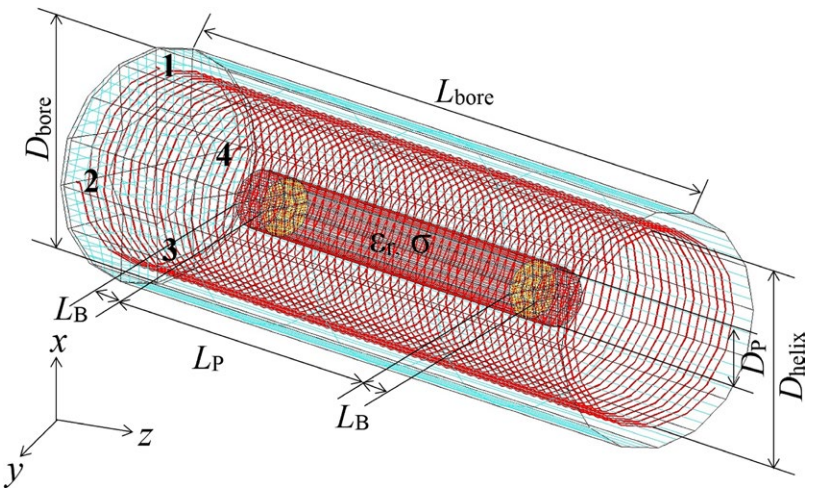

FIGURE 2 Application of the novel method for excitation of RF B_1 field in high-field ($B_0 = 3$ T) MRI systems: 3-T MRI metallic bore with an RF body coil in the form of a phantom-loaded quadrifilar helical antenna (Fig. 1) at an operating frequency of $f_0 = 127.8$ MHz, with the accepted powers at the four excitation ports (Excitations 1–4), i.e., time-average powers delivered to the ports, being P_{a1}, P_{a2}, P_{a3}, and P_{a4}, respectively. The cylindrical phantom (of length L_{P}) is terminated at both ends with small cylindrical buffers (of length L_{B}) made of the same material

3 | RESULTS, ANALYSIS, AND DISCUSSION

As the first example, we consider a 3-T MRI system in Fig. 2 ($D_{bore} = 60$ cm, $L_{bore} = 200$ cm) with a quadrifilar helical RF body coil exciter in Fig. 1 with $D_{helix} = 50$ cm, $L_{helix} = 200$ cm, $P = 12.8$ cm, $r_w = 0.1$ cm, $D_{plate} = 60$ cm, and $f_0 = 127.8$ MHz. The back-plate is located 1.5 cm away from the bore end. Dimensions of the phantom and buffers in Fig. 2 are $D_P = D_B = 15$ cm, $L_P = 100$ cm, and $L_B = 10$ cm, and the dielectric parameters are $\varepsilon_r = 81$ and $\sigma = 0.6$ S/m (saline water). The accepted powers at the ports are $P_{a1} = P_{a2} = P_{a3} = P_{a4} = 4.7$ mW.

Figure 3a shows the one-dimensional (1-D) distribution of the RCP component of the transverse RF magnetic field, B_1^+, and the left-hand CP (LCP) component, B_1^-, along the axis of the phantom (z-axis) in Fig. 2. Note that it is customary in MRI literature to refer to B as simply the magnetic field, whereas in electromagnetics B generally stands for the magnetic flux density or magnetic induction, in the units of T (tesla), and the magnetic field intensity (strength), in the units of A/m, is denoted by H.[31] In free space and nonmagnetic media, the relationship between the magnetic flux density and field intensity vectors is $\mathbf{B} = \mu_0 \mathbf{H}$ (μ_0 is permeability of free space, $\mu_0 = 4\pi\ 10^{-7}$ H/m). Note also that what we show is the RMS value of B, that is, the RMS magnitude of the complex vector $\mathbf{B}$. We observe from the figure that B_1^- is practically vanishing and that a perfect B_1^+/B_1^- ratio and a perfectly RCP B_1^+ field are achieved along the z-axis inside the saline-water phantom placed inside the quadrifilar helical RF body coil in the 3-T MRI system in Fig. 2. We also observe an almost perfect spatial uniformity (very small variation) of the transverse B_1^+ field along the z-axis.

In addition, we validate, in Fig. 3a, the MoM-SIE model and results by comparing them with those obtained by ANSYS HFSS, and an excellent agreement between the two sets of results is observed. This validation is very relevant given that the two solution approaches used are completely different, both conceptually and numerically; the MoM-SIE is a surface modeling technique that solves boundary integral

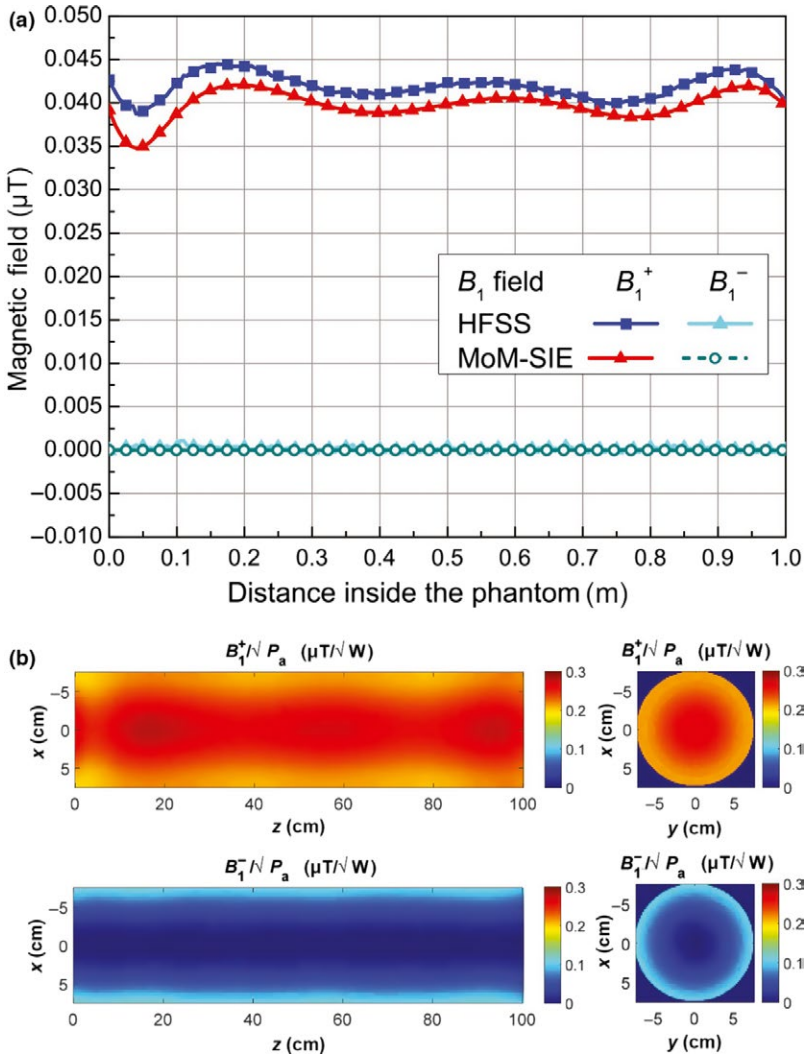

FIGURE 3 (a) 1-D distribution of the RCP component of the transverse RF magnetic field, B_1^+, and the LCP component, B_1^-, inside the saline-water phantom in the 3-T MRI system in Fig. 2 (parameters given in the text) along its axis (z-axis): comparison of the results obtained using the MoM-SIE technique and those by ANSYS HFSS commercial code. (b) 2-D RCP (transmit efficiency) and LCP normalized-field maps in the coronal ($y = 0$) and axial ($z = 50$ cm, in the middle of the phantom) cross sections of the phantom computed by ANSYS HFSS. The maximum efficiency should be compared with the efficiencies in Refs 14, 35–42

equations for currents, whereas HFSS is a volumetric modeling technique that solves partial differential equations for fields. The agreement is not perfect primarily due to a difference in the helix models—in the HFSS solution, we use thin rectangular strip elements of widths w_s, whereas in the MoM-SIE solution, the helices are modeled with cylindrical thin wire elements of radii $r_w = w_s/4$. Important details of MoM-SIE and FEM (HFSS) full-wave electromagnetic modeling of RF fields in MRI applications that enable rigorous analyses and cross-validation of the solutions in characterizations of RF coils are presented in Ref. 32.

Shown in Fig. 3b are two-dimensional (2-D) field maps of B_1^+ and B_1^- components of $\mathbf{B}_1$ in the coronal/sagittal and axial cross-sections of the phantom in Fig. 2, where we observe a very small B_1^- when compared to B_1^+ and an almost perfect RCP B_1^+ field throughout the entire phantom, as well as an almost perfect spatial uniformity of the transverse B_1^+ field throughout the phantom. More specifically, Fig. 3b shows the transmit efficiency evaluated as $B_1^+/\sqrt{P_a}$, where $P_a = P_{a1} + P_{a2} + P_{a3} + P_{a4}$ is the total accepted power for the coil, as well as the corresponding normalization of the LCP field, $B_1^-/\sqrt{P_a}$. The maximum efficiency in Fig. 3b is comparable with those reported for various coils and phantoms at 3 T, as well as 7 T in Refs 14, 35–42.

In the next example, we further analyze the magnetic field B_1 uniformity of the system in Fig. 2. Keeping all other parameters of the helical-antenna RF coil the same (as in the previous example), the diameter of the helices was increased to $D_{helix} = 58$ cm ($D_{bore} = 60$ cm, $L_{bore} = 200$ cm, $P = 12.8$ cm, $r_w = 0.1$ cm, $f_0 = 127.8$ MHz), to further improve the field uniformity in the axial plane. The length of the phantom in Fig. 2 is now $L_P = 38$ cm[6] ($D_P = D_B = 15$ cm, $L_B = 10$ cm). To simulate materials with various properties, it is filled with three different dielectrics,[6] one at the time: (A) vegetable oil ($\varepsilon_r = 2.9$, $\sigma = 0$), (B) saline water ($\varepsilon_r = 78$, $\sigma = 1.67$ S/m), and (C) water ($\varepsilon_r = 74$, $\sigma = 0$), and the buffers in Fig. 2 are made of the same material as in cases (A)–(C), respectively. Moreover, we consider four different designs of the quadrifilar helical RF coil, with: (i) $L_{helix1} = 200$ cm and $D_{plate} = 60$ cm (solid back-plate, like in the previous example), (ii) $L_{helix2} = 100$ cm, a hollow back-plate (metallic ring) with $D_{plate1} = 59$ cm and $D_{plate2} = 50$ cm, and the helical structure being positioned in the bore such that the back-plate is located at a distance of 30 cm from the bore opening, (iii) $L_{helix3} = 60$ cm, the hollow back-plate as in (ii), and the structure position such that the back-plate is 71 cm away from the bore opening, and (iv) $L_{helix3} = 50$ cm and the hollow back-plate at 73.5 cm from the bore opening.

We compare the MoM-SIE numerical results for the described helical exciters with experimental results for the 16-element quadrature birdcage coil (of diameter 27.8 cm and length 21 cm) from Ref. 6. Figure 4 shows the 1-D field distributions in the transversal direction (axial cross section) along the x-axis ($y = z = 0$) and the longitudinal direction (coronal/sagittal cross section) along the z-axis ($x = y = 0$), respectively, for the empty bore and phantoms (A)–(C). All results are normalized with respect to B_1 at the center of the phantom, as suggested in Ref. 6, and given in "arbitrary units" (a.u.). Namely, we are not able to perform comparison in absolute (nonnormalized) values and physical units because the results in Ref. 6 are given in a.u.

From Fig. 4a–b, we conclude that the numerical results for the proposed quadrifilar helical RF coil show a comparable field uniformity in the transversal direction as the birdcage coil measurements in Ref. 6, for all four phantom cases and all four helical coil lengths. Moreover, based on Fig. 4c–d, we conclude that the helical-antenna exciters with all four lengths yield remarkable improvements in the field uniformity in the longitudinal direction in all four phantom cases as compared to the birdcage coil results in Ref. 6, with the maximum field variation with respect to the mean value of the signal, δB_{max}, for $L_{helix} = 200$ cm being less than 4%. Specifically, the computed maximum field variations for empty bore and phantoms (A), (B), and (C) are $\delta B_{max} = 1.84\%$, 2.14%, 3.94%, and 3.22%, respectively. The maximum field variation when the bore is empty, for instance, reported in Ref. 6 is $\delta B_{max} = 10\%$ within 9 cm inside the phantom, whereas in our case, δB_{max} is approximately five times lower and is computed along the whole length of the phantom ($L_P = 38$ cm). In other words, with the quadrifilar helical RF coil ($L_{helix} = 200$ cm), the usable FOV is increased approximately 4.22 times, and similarly for the other three coil lengths.

We next compare our results for the vegetable oil phantom, case (A), in the longitudinal plane with the results obtained with an improved birdcage coil hardware using detached end caps as described in Ref. 7. The phantom, with $D_P = D_B = 17$ cm and $L_P = 26$ cm (all structure parameters except L_{helix}, D_P, D_B, and L_P are as in Fig. 4), is coaxially placed with respect to the bore in all four designs (i)–(iv) of the helical RF coil, and we consider two configurations: the phantom with and without dielectric buffers (in Fig. 2), respectively.

As shown in Fig. 5 [again, the results are normalized and given in a.u. to match Ref. 7], the results obtained with the shorter quadrifilar helical RF coil [designs (ii)–(iv)] are still considerably more uniform than the results in Ref. 7, even with the reported 85% improvement of the B_1 field at the service end of the birdcage with respect to that at the coil's center when detached end caps are used.[7] We also observe from the figure that the results for the phantom without buffer terminations are almost equally good. It can be concluded, therefore, that the quadrifilar helical RF coil provides a significant improvement when compared to the birdcage coil[6,7] in the longitudinal direction (even when the helical exciter is short), while the results in the transversal direction are very similar.

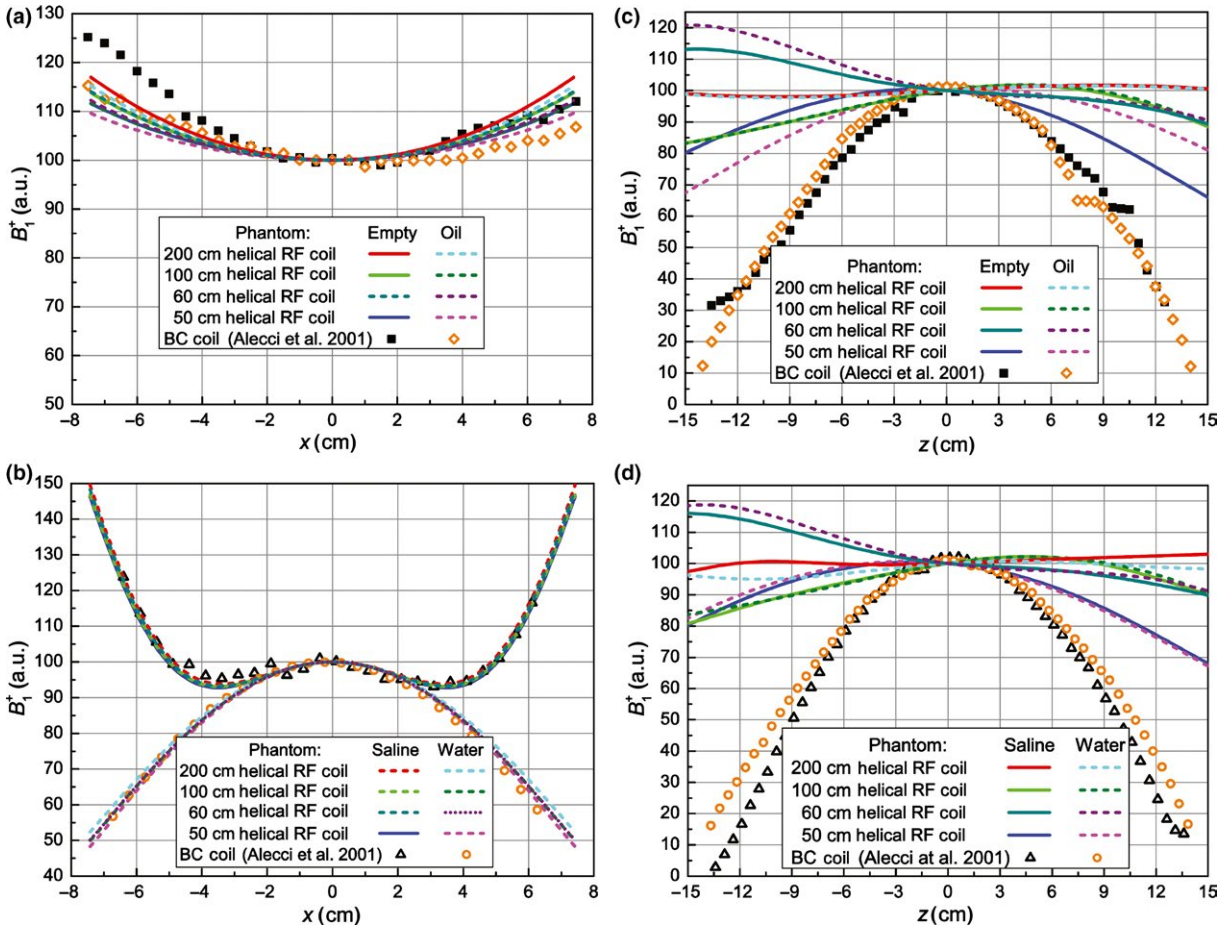

FIGURE 4 B_1^+ field in the transversal direction ($y = z = 0$) inside the 3-T MRI scanner in Fig. 2 (parameters given in the text) when the bore is (a) empty or loaded with a vegetable oil phantom—case (A) and (b) loaded with a saline-solution phantom—case (B) or a water phantom—case (C): comparison of the MoMSIE numerical results for the quadrifilar helical RF coil—of four different lengths—with experimental results for the 16-element quadrature birdcage (BC) coil from Ref. 6. (c)–(d) The same as in (a)–(b) but for B_1^+ field in the longitudinal direction ($x = y = 0$) inside the 3-T MRI scanner

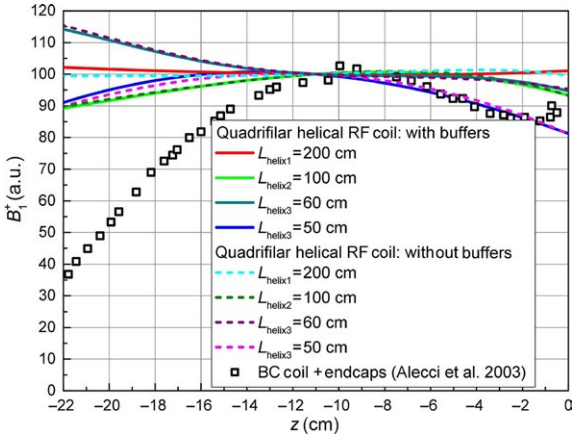

FIGURE 5 B_1^+ field in the longitudinal direction ($x = y = 0$) inside the 3-T MRI scanner in Fig. 2 (parameters given in the text) with the vegetable oil phantom: comparison of the MoM-SIE results—for four different lengths of the quadrifilar helical RF coil and for the phantom with and without buffers (Fig. 2)—with the experimental results obtained with an improved birdcage coil[7]

Next, we consider a 3-T MRI system in Fig. 2 with the same dimensions as in the first example, except for $D_{helix} = 58$ cm, $D_P = D_B = 10$ cm, and $L_p = 60$ cm ($D_{bore} = 60$ cm, $L_{bore} = 200$ cm, $L_{helix} = 200$ cm, $P = 12.8$ cm, $r_w = 0.1$ cm, $D_{plate} = 60$ cm, $L_B = 10$ cm, $f_0 = 127.8$ MHz). The parameters of the dielectric of the phantom (and the buffers) are $\varepsilon_r = 69.062$ and $\sigma = 1.5054$ S/m ($\mu_r = 1$),[16] and the accepted powers at the ports are $P_{a1} = P_{a2} = P_{a3} = P_{a4} = 6.62$ W. Figure 6 shows 2-D B_1^+ and B_1^- field maps in the coronal/sagittal and axial cross sections. As expected and observed from the figure, and based on the previous examples, the quadrifilar helical RF body coil design provides an almost perfect spatial uniformity of the transverse B_1^+ field and an almost perfect B_1^+/B_1^- ratio throughout the phantom. In terms of B_1^+ field uniformity, our design yields a notable improvement with respect to outperforms the parallel-plate waveguide design (two 25 cm wide, 60 cm long, and 6-μm-thick aluminum strips, mounted on an acrylic cylinder, 30 cm in diameter and 60 cm long) in conjunction with the embedded birdcage coil (66 cm in diameter and 68 cm long, with 16 rungs driven in quadrature) inside the 3-T MRI system described and shown in Fig. 1a in Ref.

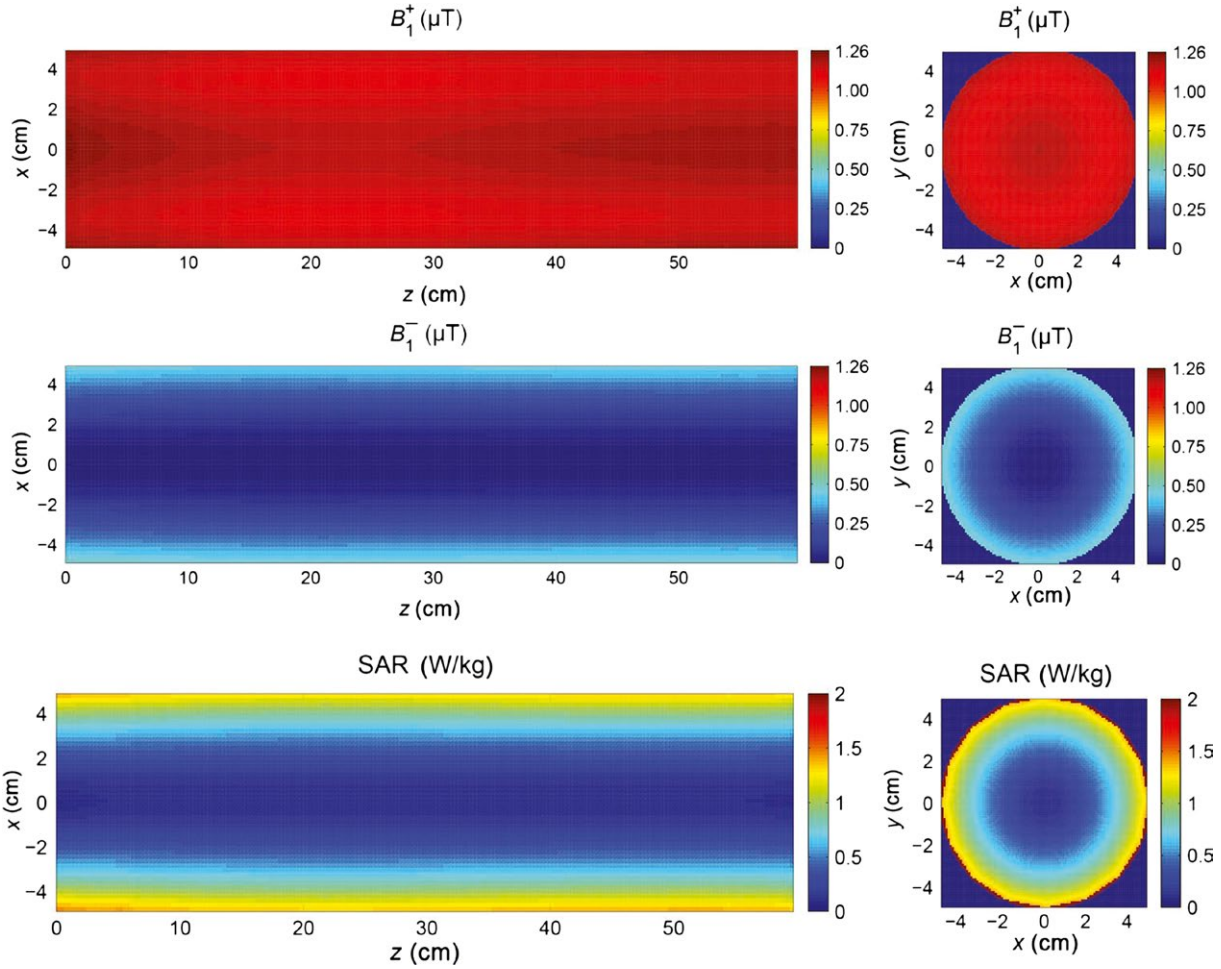

FIGURE 6 MoM-SIE 2-D field maps of B_1^+ and B_1^- fields and local SAR in the coronal ($y = 0$) and axial ($z = 30$ cm, in the middle of the phantom) cross sections of the phantom in the 3-T MRI system in Fig. 2 (parameters given in the text). The B_1^+ and B_1^- results should be compared with computed, using COMSOL Multiphysics, field maps in Fig. 2 in Ref. 16 for the parallel-plate waveguide design in conjunction with the embedded birdcage coil. The SAR results should be compared with the SAR values reported in Fig. 4(c) in Ref. 16

16. For 2-D field comparison, see the results for the 3-T MRI system shown in Fig. 2 in Ref. 16.

In addition, shown in Fig. 6 is also the distribution of the local SAR in the coronal and central axial cross sections of the phantom. It can be observed from the figure that the SAR, for the given typical or maximal total input RF power of the MRI system, would be below the allowable prescribed SAR level at every point of the phantom. The maximum SAR level we observe is 1.5 W/kg, which is within the permissible SAR range. These results are in a good agreement with the SAR range reported in Fig. 4c in Ref. 16.

In Fig. 7, we compare for uniformity the 1-D field distribution (normalized to the field level at the center of the phantom) for the quadrifilar helical-antenna RF body coil of three different lengths ($L_{\text{helix}} = 200$ cm, 100 cm, and 60 cm) with that from Ref. 16, obtained using commercial FEM code COMSOL Multiphysics V. 3.2. Here, all results are normalized with respect to B_1 at the center of the phantom and given in "arbitrary units" (a.u.) because there is no information on the power in Ref. 16, so it is impossible to

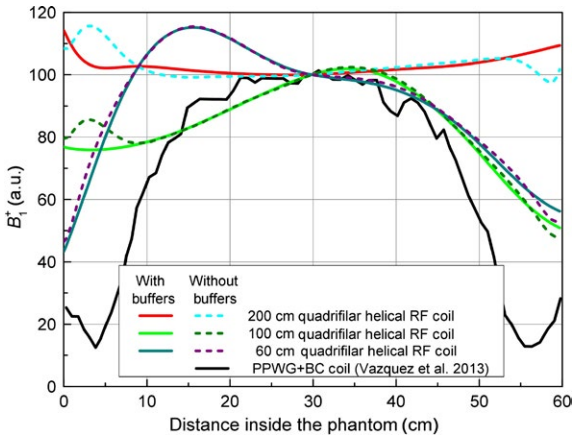

FIGURE 7 B_1^+ field inside the phantom along its longitudinal axis in the 3-T MRI system in Fig. 2 (system parameters as in Fig. 6): comparison of the MoM-SIE results for the quadrifilar helical RF body coil of three different lengths and the phantom with and without buffers (Fig. 2) with COMSOL Multiphysics results for the parallel-plate waveguide (PPWG) + birdcage (BC) coil[16] [note that the graph is directly traced from Fig. 3 in Ref. 16, where it looks differently due to a different scale; it is also qualitatively verified with the inset in Fig. 3 in Ref. 33]

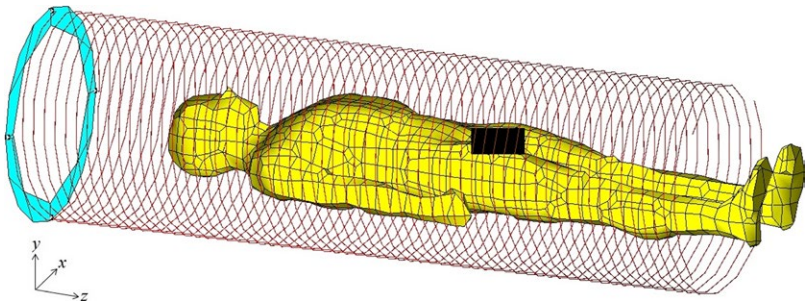

FIGURE 8 MoM-SIE simulation model of a homogeneous human body phantom (parameters given in the text) inside a 60-cm 3-T MRI bore in Fig. 2 (the bore is not shown for clarity) with the same quadrifilar helical RF body coil as in Fig. 6 but terminated with a hollow back-plate (ring)

perform comparison in absolute values. We observe from the figure that the helical RF coil with $L_{\text{helix}} = 200$ cm provides almost constant field along the phantom axis (in the longitudinal direction), as well as that the results for $L_{\text{helix}} = 200$ cm, 100 cm, and 60 cm, whether the dielectric buffers are used at the ends of the phantom (Fig. 2) or not, are considerably more uniform than those from Ref. 16 for the same phantom.

As the last example, we simulate a human body-shaped phantom inside a 60-cm 3-T MRI bore in Fig. 2 with the same quadrifilar helical RF body coil as in the previous example. For practical reasons, the helical antenna (the four helices) is terminated with a hollow back-plate (ring) with $D_{\text{plate1}} = 60$ cm and $D_{\text{plate2}} = 50$ cm, placed outside the bore, 1.5 cm away from the bore opening. A homogeneous human body MoM-SIE model of height/length $L_{\text{body}} = 184$ cm and maximum width $w_{\text{body}} = 52$ cm, filled with a lossy dielectric of averaged tissue parameters amounting to $\varepsilon_r = 31$ and $\sigma = 0.31$ S/m,[9] is placed 35 cm inside the bore (measured from the bore opening to the top of the head), as shown in Fig. 8 (the bore is not shown for the clarity of the figure). These tissue parameters are calculated in Ref. 9 by finding a volumetric average of two lossy-dielectric patient models. The accepted powers at the excitation ports 1–4 (Fig. 2) amount to $P_{\text{a1}} = 35.99$ W, $P_{\text{a2}} = 20.83$ W, $P_{\text{a3}} = 34.89$ W, and $P_{\text{a4}} = 30.48$ W, respectively.

Shown in Fig. 9 is the 1-D distribution of the B_1^+ and B_1^- transverse fields along the central axis (z-axis) of the human body model from the top of the head to the end of the torso, where we observe a very small B_1^- compared to B_1^+ and reasonable spatial uniformity of the B_1^+ field along the z-axis everywhere, from the top of the head to the end of the torso, except in the neck area ($z \approx 20$–30 cm). To mitigate the degradation in the field uniformity and circular polarization around the neck region, we add a "collar" (of the same dielectric properties as the human body phantom) around the neck, as shown in the inset of Fig. 9, and include in Fig. 9 B_1^+ and B_1^- 1-D results for the phantom model with the "collar" as well. Note that a similar idea of using a "collar" to improve the field distribution has been suggested in Ref. 34. As can also be seen from Fig. 9, the "collar" improves the field uniformity, as well as the circular polarization and B_1^+/B_1^- ratio, in and around the neck region. The maximum

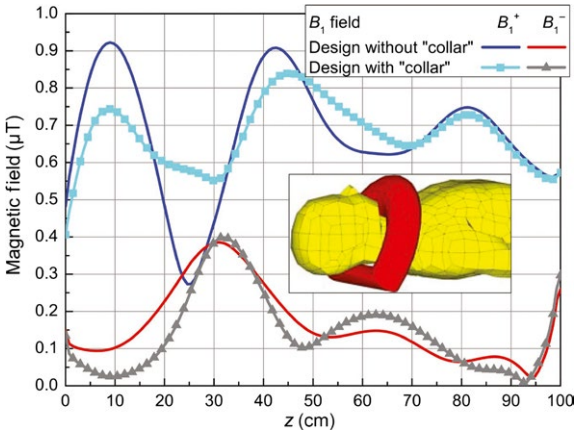

FIGURE 9 Computed 1-D distribution of B_1^+ and B_1^- efficiency inside the human body model in Fig. 8 along its central axis (z-axis) (from the top of the head to the end of the torso), without and with the dielectric "collar" (of the same dielectric properties as the phantom) around the neck, to mitigate the degradation in the field uniformity and circular polarization around the neck region. Detail of the human body model with the "collar" is shown in the figure inset

B_1^+ field variation in the neck region without the "collar" is $\delta B_{\text{max1}} = 61.5\%$ (at approximately $z = 25$ cm), whereas in the design with the "collar," it is reduced to $\delta B_{\text{max2}} = 22\%$ (at approximately $z = 30$ cm), which can be observed from Fig. 9.

Figure 10 shows 2-D B_1^+ and B_1^- field maps and SAR in the coronal and axial slices of the human body phantom in Fig. 8 with the "collar" in Fig. 9, where we observe a good overall B_1 field uniformity, circular polarization, and SAR levels throughout the phantom.

4 | CONCLUSIONS

This study has proposed a novel method for excitation of RF B_1 field in high-field ($B_0 = 3$ T) MRI systems using a subject-loaded quadrifilar helical antenna as an RF coil. Analysis, characterization, evaluation, and demonstration of the proposed quadrifilar helical exciter when situated in a 3-T MRI bore and loaded with different phantoms have been performed by extensive numerical simulations using the higher-order method of moments in the surface integral equation

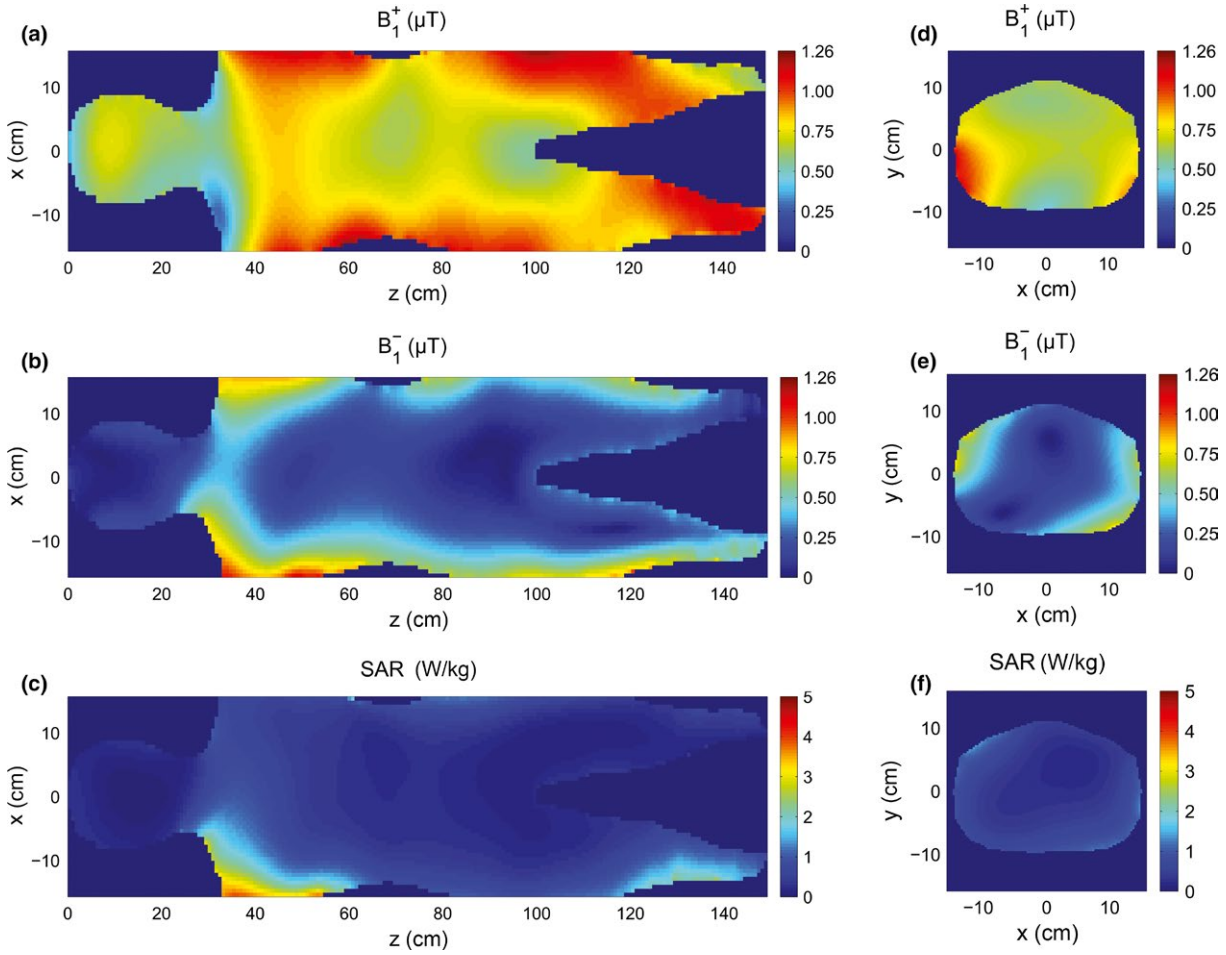

FIGURE 10 2-D B_1^+ and B_1^- field maps and SAR in (a)–(c) coronal and (d)–(f) axial ($z = 75$ cm) slices of the human body phantom in Fig. 8 with the "collar" in Fig. 9

formulation. The simulation results are fully representative and predictive of the performance of the proposed RF coil in the actual MRI bore.

The examples have shown that the helical-antenna exciter provides substantially better B_1^+ field uniformity and much larger FOV than any of the reported numerical and experimental results in literature that enable comparison. It yields a remarkable improvement in the field uniformity in the longitudinal direction as compared to the reported results, with the maximum field variation with respect to the mean value of the signal for empty bore and various phantoms being many times lower. In addition, quadrifilar helical RF body coils of different lengths can, for instance, easily provide a highly uniform B_1^+ field and excellent right-hand CP and B_1^+/B_1^- ratio within the lengths close to or exceeding practical FOV of 50 cm as defined by B_0 field uniformity and gradient coil dimensions. Even the lengths of 100 cm can easily be covered, which might not be practical at the moment but is certainly interesting and noteworthy. The transmit efficiencies evaluated as $B_1^+/\sqrt{P_a}$, with P_a standing for the total accepted power for the coil, are comparable with those reported for various coils and phantoms at 3 T, as well as 7 T. The SAR distributions and local SAR values in the phantoms are in agreements with the SAR distributions and ranges reported for similar 3-T systems. The simulation results for the homogeneous human body phantom inside the quadrifilar helical RF body coil at 3 T have shown a good overall B_1 field uniformity, circular polarization, and SAR levels throughout the phantom.

Our future work will include measurements and experimental testing of the novel coil in a 3-T MRI scanner, human–phantom CEM studies including heterogeneous numerical phantoms, further quantitative comparative studies relative to the corresponding existing RF coils at 3 T, further improvements of the designs, as well as designs and demonstrations of helical-antenna RF coils at fields other than 3 T, namely, at ultrahigh fields.

ACKNOWLEDGMENTS

This work was supported by the National Science Foundation under grant ECCS-1307863 and by the Serbian Ministry of Education, Science, and Technological Development under grant TR-32005.

REFERENCES

1. Hoult DI, Lauterbur PC. The sensitivity of the zeugmatographic experiment involving human samples. *J Magn Reson*. 1979;34:425–433.
2. Callaghan PT. *Principles of Nuclear Magnetic Resonance Microscopy*. New York: Oxford University Press; 1993.
3. Liang ZP, Lauterbur PC. *Principles of Magnetic Resonance Imaging: A Signal Processing Perspective*. New York: IEEE Press; 2000.
4. Uğurbil K. Magnetic resonance imaging at ultrahigh fields. *IEEE Trans Biomed Eng*. 2014;61:1364–1379.
5. Hayes CE, Edelstein WA, Schenck JF, Mueller OM, Eash M. An efficient, highly homogeneous radiofrequency coil for whole-body NMR imaging at 1.5 T. *J Magn Reson*. 1985;63:622–628.
6. Alecci M, Collins CM, Smith MB, Jezzard P. Radio frequency magnetic field mapping of a 3 T birdcage coil: experimental and theoretical dependence on sample properties. *Magn Reson Med*. 2001;46:379–385.
7. Alecci M, Collins CM, Wilson J, Liu W, Smith MB, Jezzard P. Theoretical and experimental evaluation of detached endcaps for 3 T birdcage coils. *Magn Reson Med*. 2003;49:363–370.
8. Vaughan JT, Adriany G, Snyder CJ, Tian J, Thiel T, Bolinger L, et al. Efficient high-frequency body coil for high-field MRI. *Magn Reson Med*. 2004;52:851–859.
9. Van den Berg CA, Van den Bergen B, Van de Kamer JB, Raaymakers BW, Kroeze H, Bartels LW, et al. Simultaneous B+ homogenization and specific absorption rate hotspot suppression using a magnetic resonance phased array transmit coil. *Magn Reson Med*. 2007;57:577–586.
10. Tian J, DelaBarre L, Strupp J, Zhang J, Pfeuffer J, Hamm M, et al. Searching for the optimal body coil design for 3T MRI. In: Proceedings of the 21st Annual Meeting, International Society for Magnetic Resonance in Medicine, Salt Lake City, Utah, USA; 2013. pp 2746.
11. Alsop DC, Connick TJ, Mizsei G. A spiral volume coil for improved RF field homogeneity at high static magnetic field strength. *Magn Reson Med*. 1998;40:49–54.
12. Zhang B, Wiggins G, Duan Q, Sodickson DK. Design of a patch antenna for creating traveling waves at 7 tesla. In: Proceedings of the 17th Scientific Meeting, International Society for Magnetic Resonance in Medicine, Honolulu, HI, USA; 2009: pp 4746.
13. Mallow J, Herrmann T, Kim KN, Stadler J, Mylius J, Brosch M, et al. Ultrahigh field MRI for primate imaging using the travelling-wave concept. *Magn Reson Mater Phy*. 2012;26:389–400.
14. Andreychenko A, Kroeze H, Klomp DW, Lagendijk JJ, Luijten PR, van den Berg CA. Coaxial waveguide for travelling wave MRI at ultrahigh fields. *Magn Reson Med*. 2013;70:875–884.
15. Andreychenko A, Bluemink JJ, Raaijmakers AJ, Lagendijk JJ, Luijten PR, van den Berg CA. Improved RF performance of travelling wave MR with a high permittivity dielectric lining of the bore. *Magn Reson Med*. 2013;70:885–894.
16. Vazquez F, Martin R, Marrufo O, Rodriguez AO. "Travelling wave magnetic resonance imaging at 3T". *J Appl Phys [Online]*. 2013;114:064906. Available: http://dx.doi.org/10.1063/1.4817972.
17. Tonyushkin A, Konyer NB, Ranzani LM, Popovich Z, Noseworthy MD, Kiruluta AJM. Improvement of traveling wave performance at 3T using high dielectric rods. In: Proceedings of the 55th Experimental Nuclear Magnetic Resonance Conf., Boston, MA, USA; 2014.
18. Tonyushkin A, Konyer NB, Noseworthy MD, Kiruluta AJM. Quasi-static traveling wave imaging on a clinical 3T MRI system. In: Proceedings of the 21st Annual Meeting, International Society for Magnetic Resonance in Medicine, Salt Lake City, Utah, USA; 2013, p 4883.
19. Eustace SJ, Nelson E. Whole body magnetic resonance imaging; a valuable adjunct to clinical examination. *BMJ : British Medical Journal*. 2004;328(7453):1387–1388.
20. Notaros BM, Ilić MM, Tonyushkin AA, Sekeljic NJ, Athalye P. Quadrifilar helical antenna as a whole-body traveling-wave RF coil for 3T and 7T MRI. In: Proceedings of the 23rd Annual Meeting, International Society for Magnetic Resonance in Medicine, Toronto, Ontario, Canada; 2015, p 1825.
21. Athalye PS, Sekeljic NJ, Ilic MM, Tonyushkin AA, Notaros BM. 2015. Using Subject-Loaded Quadrifilar Helical Antennas as RF Body Coils at 3 T. 10th Biennial 2015 Minnesota Workshop on High and Ultra-High Field Imaging, October 1-3, 2015, Minneapolis, MN.
22. Athalye PS, Sekeljic NJ, Ilic MM, Tonyushkin AA, Kiruluta AJM, deVan Moortele PF, et al. 2015. Long and short monofilar and quadrifilar helical antenna RF coils at 7 T. Invited Presentation. 10th Biennial 2015 Minnesota Workshop on High and Ultra-High Field Imaging, Minneapolis, MN.
23. Athalye PS, Ilic MM, de Van Moortele PF, Kiruluta AJM, Notaros BM. Multi-Channel Helical-Antenna Inner-Volume RF Coils for Ultra-High-Field MRI Scanners. In: Proceedings of the 24th Annual Meeting, International Society for Magnetic Resonance in Medicine, Singapore; 2016: p 2127.
24. Ilić MM, Tonyushkin AA, Sekeljic NJ, Athalye P, Notaros BM. RF excitation in 7 T MRI systems using monofilar axial-mode helical antenna. In: Proceedings of the 2015 IEEE International Symposium on Antennas and Propagation, Vancouver, BC, Canada, July 19-25; 2015: pp 1346–1347.
25. Notaros BM. Higher order frequency-domain computational electromagnetics. Invited review paper, Special Issue on Large and Multiscale Computational Electromagnetics. *IEEE Trans Antennas Propagat*. 2008;56:2251–2276.
26. Djordjevic M, Notaros BM. Double higher order method of moments for surface integral equation modeling of metallic and dielectric antennas and scatterers. *IEEE Trans Antennas Propagat*. 2004;52:2118–2129.
27. Djordjević AR, Zajić AG, Ilić MM, Stuber G. "Optimization of helical antennas" [Antenna Designer's Notebook]. IEEE Antennas Propagat Magazine. 2006;48:107–115.
28. WIPL-D Pro v11, WIPL-D d.o.o. 2014. Available: http://www.wipl-d.com. Accessed June 1, 2015.
29. HFSS, ANSYS® Electromagnetics Suite 15.0.7, ANSYS, Inc. Available: http://www.ansys.com. Accessed June 1, 2015.
30. Ohliger MA, Sodickson DK. An introduction to coil array design for parallel MRI. *NMR Biomed*. 2006;19:300–315.
31. Notaros BM. *Electromagnetics*. New Jersey: PEARSON Prentice Hall; 2010.
32. Ilić MM, Perović I, Tonyushkin AA, Athalye P, Šekeljić N, Notaroš BM. Full-wave frequency-domain electromagnetic modelling of RF fields in MRI applications". In: Proceedings of the 2015 IEEE International Symposium on Antennas and Propagation, Vancouver, BC, Canada, July 19-25, 2015; pp 971–972.
33. Vazquez F, Martin R, Marrufo O, Rodriguez AO. 2013. "Travelling wave magnetic resonance imaging at 3 Tesla".Medical Physics [arXiv: 1301.3426v1].
34. Yang QX, Rupprecht S, Luo W, Sica C, Herse Z, Wang J, et al. Radiofrequency field enhancement with high dielectric constant (HDC) pads in a receive array coil at 3.0 T. *J Magn Reson Imag*. 2013;38:435–440.
35. Brink WM, Versluis MJ, Peeters JM, Börnert P, Webb AG. "Passive radiofrequency shimming in the thigh at 3 Tesla using high permittivity material and body coil receive uniformity correction". *Magn Reson Med*. 2015. doi: 10.1002/mrm.26070.
36. Brown R, Lakshmanan K, Madelin G, Alon L, Chang G, Sodickson DK, et al. "A flexible nested sodium and proton coil array with wideband matching for Knee cartilage MRI at 3T". *Magn Reson Med*. 2015. doi: 10.1002/mrm.26017.
37. Guérin B, Gebhardt M, Serano P, Adalsteinsson E, Hamm M, Pfeuffer J, et al. Comparison of simulated parallel transmit body arrays at 3 T using excitation uniformity, global SAR, local SAR, and power efficient metrics. *Magn Reson Med*. 2015;73:1137–1150.
38. Pohmann R, Speck O, Scheffler K. Signal-to-noise ratio and MR tissue parameters in human brain imaging at 3,4, and 9.4 Tesla using current receive coil arrays. *Magn Reson Med*. 2015;75:801–809.
39. Hoffmann J, Shajan G, Budde J, Scheffler K, Pohmann R. Human brain imaging at 9.4 T using a tunable patch anetnna for transmission. *Magn Reson Med*. 2013;69:1494–1500.

40. Brunner DO, Paška J, Froehlich J, Pruessmann KP. Traveling-wave RF shimming and parallel MRI. *Magn Reson Med*. 2011;66:290–300.
41. Andreychenko A, Kroeze H, Boer VO, Lagendijk JJ, Luijten PR, van den Berg CA. Improved steering of the RF field of traveling wave MR with a multimode, coaxial waveguide. *Magn Reson Med*. 2014;71:1641–1649.
42. Zhang B, Sodickson DK, Lattanzi R, Duan Q, Stoeckel B, Wiggins GC. Whole body traveling wave magnetic resonance imaging at high field strength: homogeneity, efficiency, and energy deposition as compared with traditional excitation mechanisms. *Magn Reson Med*. 2012;67:1183–1193.